ACS APPLIED MATERIALS & INTERFACES

Research Article

www.acsami.org

High Volumetric Energy Density Hybrid Supercapacitors Based on Reduced Graphene Oxide Scrolls

Janardhanan R. Rani,[†,∥] Ranjith Thangavel,[‡,∥] Se-I Oh,[†] Jeong Min Woo,[†] Nayan Chandra Das,[†] So-Yeon Kim,[†] Yun-Sung Lee,[‡] and Jae-Hyung Jang*[,†,§]

[†]School of Electrical Engineering and Computer Science, Gwangju Institute of Science and Technology, Gwangju 61005, South Korea

[‡]Faculty of Applied Chemical Engineering, Chonnam National University, Gwangju 61186, South Korea

[§]Research Institute for Solar and Sustainable Energies, Gwangju Institute of Science and Technology, Gwangju 61005, South Korea

Supporting Information

ABSTRACT: The low volumetric energy density of reduced graphene oxide (rGO)-based electrodes limits its application in commercial electrochemical energy storage devices that require high-performance energy storage capacities in small volumes. The volumetric energy density of rGO-based electrode materials is very low due to their low packing density. A supercapacitor with enhanced packing density and high volumetric energy density is fabricated using doped rGO scrolls (GFNSs) as the electrode material. The restacking of rGO sheets is successfully controlled through synthesizing the doped scroll structures while increasing the packing density. The fabricated cell exhibits an ultrahigh volumetric energy density of 49.66 Wh/L with excellent cycling stability (>10 000 cycles). This unique design strategy for the electrode material has significant potential for the future supercapacitors with high volumetric energy densities.

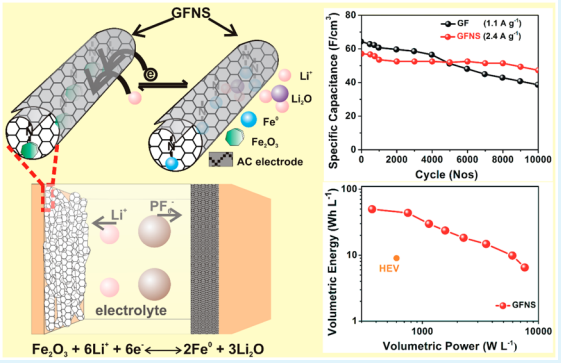

KEYWORDS: *rGO, Fe_2O_3, scrolls, hybrid supercapacitor, volumetric energy density*

1. INTRODUCTION

The miniaturization of electronic devices demands the development of high performance energy storage devices in small volumes, i.e., fabricating supercapacitors with high volumetric energy density. Recently, various novel high performance devices such as supercapacitors,[1] potassium ion based batteries,[2] dual ion batteries,[2−6] Li ion batteries,[7] sodium hybrid capacitors,[8,9] etc., are studied and developed. Due to their high gravimetric energy density, reduced graphene oxide (rGO)-based supercapacitors are promising candidates for energy storage applications.[10,11] The highly porous nature of rGO-based electrodes offers a large specific surface area and favors ion diffusion that results in high gravimetric energy density, good rate performance, and cycling stability.[12,13] However, the significant disadvantage of rGO-based electrode materials is the low packing density of graphene (<0.5 g/cm^{-3}), and this results in poor volumetric energy density, which severely limits their future application in lightweight portable devices, particularly in mobile electronics and electric vehicles.[14−16]

The volumetric energy density of most commercially available supercapacitors is in the range of 5−8 Wh/L, which is significantly lower than that of lead-acid batteries (50−90 Wh/L).[17] Recently, in order to overcome the poor volumetric energy density, several methods have been used to engineer rGO electrode materials and to utilize them in fabricating supercapacitors with high volumetric energy densities. The three-dimensional (3D) porous graphene network prepared using commercial Ni foams as substrates has been used recently; however, the large pore size of the porous graphene results in very low volumetric energy densities.[18] Compactly interlinked graphene nanosheets, which are produced using the evaporation-induced drying of a graphene hydrogel, have demonstrated volumetric energy densities of up to 13.1 Wh/L.[19] Pham et al. reported electrochemically reduced graphene oxide (ERGO) hydrogels for supercapacitor applications.[20] Using the electrophoretic deposition of GO onto nickel (Ni) foam, the volumetric energy density of 6 Wh/L was demonstrated. Xu et al. reported a 3D holey graphene framework with a hierarchical porous structure that delivers a volumetric energy density of 49 Wh/L.[21] A pillared graphene framework consisting of graphene fragments between graphene sheets, which were prepared via the thermal reduction of ozone-treated GO, exhibited a volumetric energy density of 27 Wh/L.[22]

While the supercapacitors based on graphene hydrogels, 3D holey graphene frameworks, and pillared graphene frameworks have exhibited higher volumetric energy densities, the techniques used to synthesize these materials are complex and time-consuming. Hence, it is necessary to develop a facile method for

Received: March 8, 2017
Accepted: June 14, 2017
Published: June 14, 2017

DOI: 10.1021/acsami.7b03299
ACS Appl. Mater. Interfaces 2017, 9, 22398−22407

synthesizing rGO-based electrodes with high volumetric energy densities. One feasible method of enhancing the volumetric energy density is to enhance the packing density of the rGO sheets. The packing density can be easily enhanced through densely stacking rGO sheets, but this significantly affects the volumetric energy density of the devices because it is difficult for the electrolyte to access the interspace area of the graphene sheets, thereby reducing their volumetric energy density. Therefore, it is challenging to design and engineer rGO sheets to have dense packing without restacking and aggregation of the rGO sheets and to exhibit high volumetric energy density. Here, a novel strategy is introduced that prevents restacking and increases the packing density through synthesizing doped rGO scrolls. In order to synthesize the rGO scrolls, metal oxide (Fe_2O_3) particles are attached to the rGO sheets and annealed in N_2 ambient air. The attachment of heavy metal oxide particles onto the rGO sheets results in the rGO sheets scrolling and Fe_2O_3-wrapped nitrogen-doped rGO scrolls are formed (hereafter, referred to as GFNSs).

The GFNSs not only prevent restacking of the rGO sheets but also increase the packing density. The role of nitrogen annealing is to strengthen the rGO-Fe_2O_3 bonding through creating active nucleation sites on the rGO sheets for the attachment of the Fe_2O_3 particles. Furthermore, the scroll structure prevents the detachment of Fe_2O_3 particles from rGO, which in turn provides excellent stability to the fabricated supercapacitor. Additionally, the presence of Fe_2O_3 particles increases the packing density and effectively reacts with the electrolyte, thereby increasing the electrode conductivity, which provides higher pseudocapacitance for the hybrid supercapacitor. Thus, GFNSs have characteristics of open ends/edges, and adjustable interlayer distances, which enhance the electrolyte accessibility.[23−25] During the charge/discharge cycle, Li ions are intercalated/deintercalated. During this intercalation/deintercalation process, a large volume expansion of active material occurs, which introduces a nonuniform strain in the scroll structure. In order to reduce this nonuniform strain, the layers are self-adjusted through interlayer sliding to achieve a minimum energy configuration. Schmidt and co-workers developed a strain-released rolled-up nanotechnology to prepare bilayer nanoscrolls that effectively buffered the swelling stress during Li^+ ion insertion/extraction and enhanced the cycling stability.[26,27] It has also been reported that the interlayer spacing of scrolls self-adjusts, buffering the swelling stress.[23] Thus, scrolls with robust outer walls and expandable inner space can provide stable structures for volume swelling/shrink during ion insertion/extraction, leading to long-term cycling stability.

Note that the proposed supercapacitor exhibits a very high volumetric energy density of 49.66 Wh/L and an excellent cycling stability of more than 10 000 cycles. The GFNSs offer a promising design strategy for optimizing the electrochemical performance of hybrid materials.

2. EXPERIMENTAL SECTION

2.1. Preparation of GO. GO was synthesized using a modified Hummer's method[28] via oxidizing graphite powder: 20 g of graphite powder, 10 g of $K_2S_2O_8$, and 10 g of P_2O_5 were mixed and added to a solution of 30 mL of concentrated H_2SO_4 at 80 °C, and the mixture was allowed to react for 6 h. Graphite powder, $K_2S_2O_8$, and P_2O_5 were purchased from Sigma-Aldrich Korea (99.9% purity). Then, the product was washed with distilled water until the pH value become neutral; this was followed by filtration. The oxidized graphite was added to 460 mL of H_2SO_4 at 0 °C using an ice bath, and then 60 g of $KMnO_4$ was added gradually with continuous stirring and cooling to maintain the temperature below 35 °C. Then, 920 mL of distilled water was added after 2 h and the mixture was maintained for 2 h; 2.8 L of distilled water and 50 mL of 30% H_2O_2 were added until the solution color turned yellow. In order to remove the metal ions, the solution was centrifuged and washed with 10% HCl, and then distilled water. A two-week dialysis was performed in order to completely remove the metal ions. Finally, the resulting GO solution was dried at 90 °C overnight in order to obtain the GO powder.

2.2. Preparation of Fe_2O_3 Encapsulated within rGO Scrolls. Fe_2O_3 powders purchased from (Sigma-Aldrich) are used for the scroll preparation. Sizes of the Fe_2O_3 particle are in the range 50−100 nm. For the synthesis of the Fe_2O_3 encapsulated within the rGO scrolls, GO (0.3 g) was dispersed in 30 mL of water and 0.1 g of Fe_2O_3 was added to the dispersion. This mixture was suspended in water via sonication for 60 min using an ultrasonic reactor operated at a frequency of 33 kHz. The mixture was centrifuged at 10 000 rpm for 10 min, which resulted in a homogeneous suspension, followed by filtering. The sonication centrifugation and filtering were conducted multiple times. The resulting solution was dried at 90 °C overnight in order to obtain the powder. The powder was further mixed in an agate mortar for 30 min, and it was then annealed at 400 °C in a nitrogen ambient for 2 h. The resulting powder consisted of Fe_2O_3 encapsulated within the rGO scrolls, which was confirmed using scanning electron microscope images (Figure 2a). The nitrogen-annealed Fe_2O_3 encapsulated by rGO scrolls are referred to as GFNSs, and they are used for the supercapacitor fabrication.

2.3. Preparation of the rGO-Fe_2O_3 Composites. For the comparative study, Fe_2O_3-embedded rGO was prepared through mixing 0.3 g of GO and 0.1 g of Fe_2O_3 powder in an agate mortar and annealing at 400 °C in air. The resulting powder is referred to as GF and was also used for cell fabrication.

For the comparison of the Raman, X-ray powder diffraction (XRD), and X-ray photoelectron spectroscopy (XPS) measurements, the rGO obtained via annealing GO powder at 400 °C was also used. The morphological, structural, and compositional properties of the GFNS and GF powders were investigated using scanning electron microscopy (SEM) (JEOL, JSM-6700F), high resolution transmission electron microscopy (HRTEM)/selective area electron diffraction (SAED) (JEM.ARM.200F), Raman spectroscopy (via a Raman microscope), X-ray diffraction (XRD) (Rigaku-D/MAX-2500H), and X-ray photoelectron spectroscopy (XPS) measurements. The measurement of the nitrogen adsorption isothermal was conducted at 77 K using a low temperature nitrogen adsorption surface area analyzer (ASAP 2020, Micromeritics Instrument Corp., USA).

2.4. Cell Fabrication. Composite anodes were formulated with 75% active materials (GFNS, GF), 15% Ketzen black (KB), and 10% teflonized acetylene black (TAB) using ethanol. Then, the slurry was pressed on a 200 mm^2 nickel steel mesh current collector and dried at 160 °C for 4 h in a vacuum oven. The same procedure was repeated to fabricate the activated carbon (AC) electrodes. For cell fabrication, the mass of the active material used is 2.5 mg/cm^2. The test cells were constructed in an argon-filled glovebox through compressing the GFNS electrode and AC counter electrode, which were separated by a porous polypropylene film (Celgard 3401, USA) and electrolyte solution of 1 M $LiPF_6$ in 1:1 ethylene carbonate (EC)/dimethyl carbonate (DMC). The fabricated cells were named GFNS/AC and GF/AC. The electrochemical performances of the hybrid supercapacitor cells were measured using CR2032 coin cells in the range of 0−3 V using a battery tester (WBCS 3000, WonATech, Korea). The cyclic voltammetry (CV) measurements were conducted at a scan rate ranging from 5 to 50 mV/s, and the galvanostatic charge/discharge (GCD) cycling of the cells was also performed in the current density range from 0.26 to 4.5 A/g. The electrochemical impedance spectroscopy (EIS) measurement was performed in the frequency range of 100 kHz to 100 MHz.

3. RESULTS AND DISCUSSION

A schematic of the preparation procedure for the GFNS cell is depicted in Figure 1.

DOI: 10.1021/acsami.7b03299
ACS Appl. Mater. Interfaces 2017, 9, 22398−22407

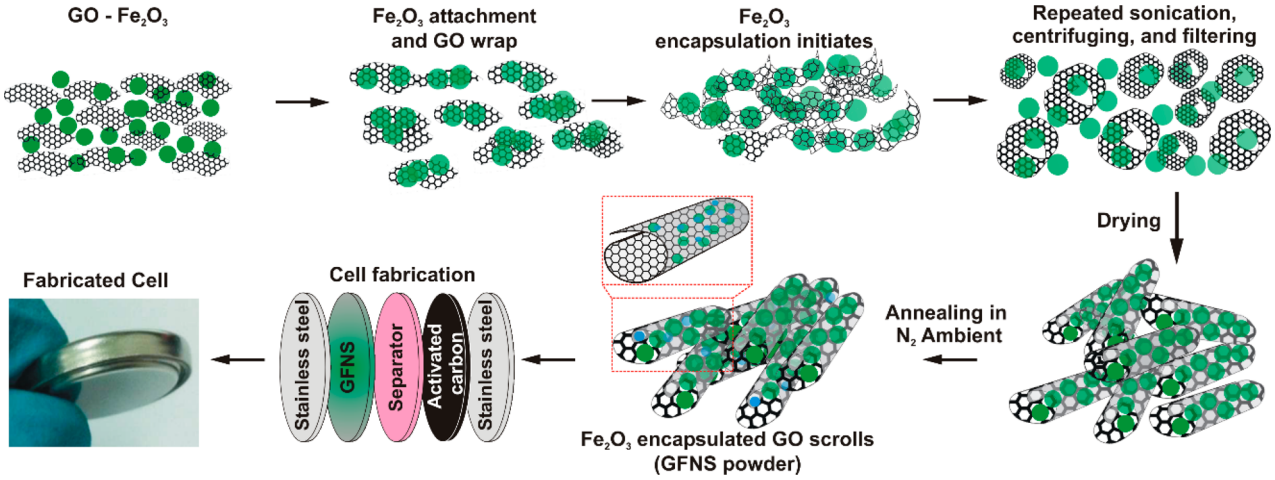

Figure 1. Schematic diagram illustrating the synthesizing procedure of the GFNS and the supercapacitor cell.

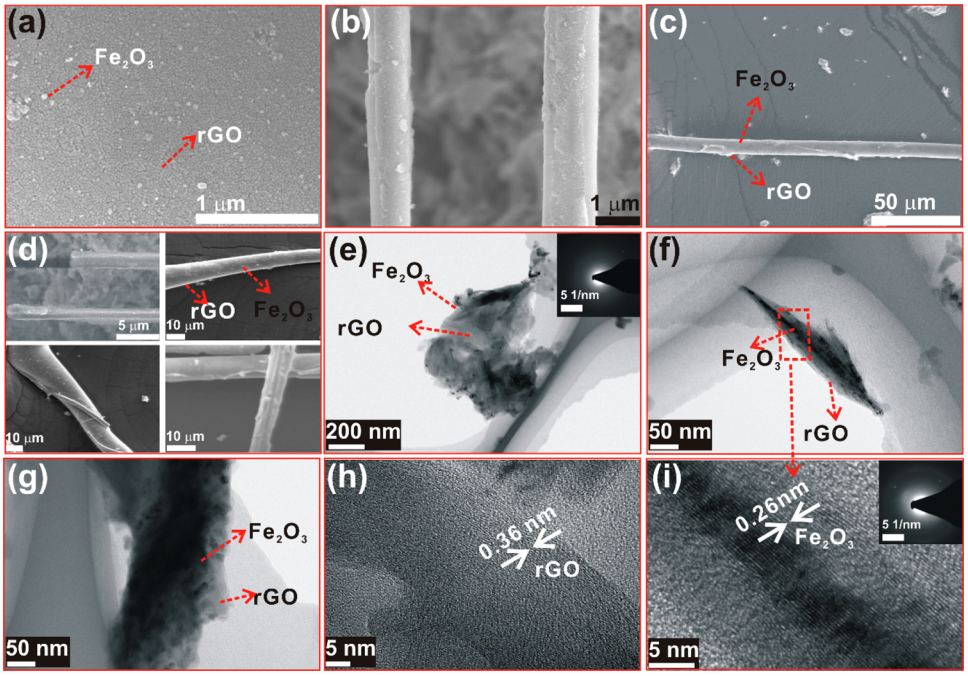

Figure 2. SEM images of (a) GF and (b–d) GFNS. Magnified images of the scrolls are presented in (d). HRTEM images of (e) GF and (f–i) GFNS. The SAED patterns of the GF and GFNS are depicted in the insets of (e) and (i), respectively. rGO and Fe_2O_3 are marked in the figures.

The morphology and the attachment of Fe_2O_3 particles on GF and GFNS samples are analyzed using SEM and TEM/HRTEM images. The SEM and HRTEM images of the GF, as seen in Figure 2a,e, respectively, clearly reveal that the Fe_2O_3 particles were attached to the flat rGO sheets. The morphology of the GFNS sample, as observed from the SEM images in Figure 2b–d, confirms the formation of the rGO scrolls in which Fe_2O_3 is encapsulated. It should be noted that the scroll formation was not observed in the GF sample.

The GFNS samples are formed by rolling rGO layers in one or more directions.[29] Scrolling occurs because Fe_2O_3 particles attached onto the rGO sheets make rGO's planar structure extremely unfavorable to maintain. A detailed discussion regarding the formation of the GO scrolls has been given in the Supporting Information (section S1) and also reported in our previous work.[30] From the TEM images, it is clear that the Fe_2O_3 particles are wrapped by rGO scrolls. The sizes of the synthesized rGO sheets are in a wide range, and the resulting scrolls have various sizes and diameters. Larger rGO sheets transform to longer scrolls with a larger diameter, while the smaller rGO sheets transform to the shorter scrolls.

In addition, the HRTEM images of the GFNS, as seen in Figure 2f–i, clearly depict the scroll structure. The lattice fringes with a *d*-spacing of 0.36 nm observed in Figure 2h correspond to the hexagonal lattice of graphene.[31] The HRTEM image in Figure 2i presents the Fe_2O_3 encapsulated by rGO scrolls. The fringes with a space of 0.26 nm can be indexed as a (104) lattice plane of Fe_2O_3.[32] The energy-dispersive X-ray (EDX) spectrum of a single scroll indicates the existence of Fe, C, N, and O without impurities; this is presented in Supporting Information Figure S1. The SEM and HRTEM images of the GFNS confirm that Fe_2O_3 is well-encapsulated within the rGO scrolls.

The Raman analyses (Figure S2a) of GF and GFNS depict the spectral features of rGO, which exhibited G peaks at 1590 and 1594 cm^{-1}, respectively.[33] It should be noted that the GFNS exhibited additional peaks at 1860 and 2080 cm^{-1}.

DOI: 10.1021/acsami.7b03299
ACS Appl. Mater. Interfaces 2017, 9, 22398–22407

The peak at 1860 cm^{-1} was ascribed to the combination of the in-plane transverse acoustic (iTA) and the longitudinal optical (LO) phonons such as iTALO, which are not Raman active modes in graphene, but are active in carbon nanotubes due to their peculiar structure; these are known as the M band.[34] The M band is active in the GFNS due to its scroll structure that exhibits properties similar to those of carbon nanotubes. The C−N−Fe bonding groups cause the stretching modes near 2080 cm^{-1}.[35]

The porosity of GF and GFNS was investigated using N_2 adsorption−desorption measurements at 77 K, and the pore size distributions (PSDs) of GFNS and GF are presented in Supporting Information Figure S2b,c, respectively. The GFNS have well-defined micropores (approximately 2.0 nm) and mesopores. The GFNS exhibited a comparatively narrower pore size distribution than the GF sample. The mesopore volume was determined through extracting the micropore volume, which was obtained from *t*-plot analyses, from the total pore volume. The mesopore volumes of the GFNS and GF samples were 0.03638 and 0.071 $cm^3\ g^{-1}$, respectively. It should be noted that the well-defined mesopores (uniform mesopores with narrow size distribution) in the GFNS provide better accessibility for the electrolyte. The Brunauer−Emmett−Teller (BET) surface area measurements are shown in Figure S2d,e. The nitrogen adsorption/desorption plot of the samples at 77.4 K shows the type IV adsorption isothermal curve with a hysteresis loop. It can be clearly observable that GFNS have higher surface area compared to GF samples. It is worth to point out here that the BET surface area is not necessarily the actual accessible sites to electrolyte ions. The device performance cannot be only evaluated by the BET surface area, but porosity and pore size distribution are also important factors determining the overall performances.

In order to confirm the bonding between the Fe_2O_3 and the rGO sheets, XRD pattern (Figure S2f), the XPS survey spectrum (Figure S3a), the high resolution C 1s XPS spectra (Figure S3b,c), N 1s XPS spectra (Figure S3d), and Fe 2p XPS spectra (Figure S3e,f) of the GF and GFNS powders were analyzed. All spectra were deconvoluted, and the resulting binding energy (BE) peaks are described in Supporting Information Table S1. The C 1s XPS results of the GFNS clearly indicate that Fe_2O_3 was attached to the rGO via nitrogen through C−N−Fe bonding.

The N 1s spectra exhibited peaks at around 397.2 eV (pyridinic-N), 398.9 eV (N−Fe bonding), 401 eV (quaternary-N_3, N atoms replace the C atoms in the graphene hexagonal ring), and 402.4 eV (oxidized nitrogen).[36] Compared with the reported value (398.2 eV), a slight shift to the lower BE was observed for the pyridinic-N peak. This shift indicates possible interactions between N and Fe.[36] Thus, the C 1s, N 1s, and Fe 2p XPS spectra provide clear evidence of the C−N−Fe bonding. The energy storage behavior of hybrid supercapacitors mainly depends on the mass balance between the individual electrodes. This is because the applied current in a hybrid supercapacitor will split based on the separate capacitive performances of the electrodes. In order to balance the current flow in both electrodes, it is critical that the mass loading of the electrodes be adjusted, during the fabrication of hybrid supercapacitors, based on the electrochemical performance of such electrodes in a single electrode configuration (Li/GFNS and Li/AC, where metallic lithium acts as counter and reference electrode).[37,38] In our study, we have fabricated Li/GFNS and Li/AC cells; typical charge−discharge curves of Li/GFNS and Li/AC cells at 2 A/g are shown in the Supporting Information (Figure S4). From the charge−discharge studies, discharge capacity values of ∼150 and 50 mAh/g are obtained for GFNS and AC electrodes, respectively. Thus, in the present study, a hybrid capacitor was constructed with GF/GFNS-AC electrodes with a GF/GFNS:AC mass ratio of 1:3.

The lithium storage nature of a GFNS electrode is analyzed in a half-cell configuration with lithium metal as the reference in the anodic region (Figure S5). Figure S5b depicts the charge−discharge voltage profiles of the GFNS electrode in a Li half-cell over 0−3.0 V at a current density of 100 mA g^{-1}, delivering a discharge capacity of 830 mAh g^{-1}. Although the Coulombic efficiency was 94% in the first cycle, it increased with further cycling and stabilized at 97% in the fifth cycle. The GFNS electrode exhibited excellent cycling stability, as depicted in Figure S5c, which is essential for an electrode material for hybrid capacitor application. Note that the Li storage capacity of the GFNS is higher than those recently reported (Table S2). The high capacity and excellent stability resulted from an enhancement in the electron transfer process between the electrode and electrolyte and a faster ion transfer between the electrode and electrolyte, which will be discussed again later. In the GFNS, the Li ions are stored at the interface between Fe_2O_3 and walls of the scrolls, which favors the high storage capacity. A schematic illustrating the Li ions stored between Fe_2O_3 and the walls of the scrolls is depicted in Figure S5d.

The CV measurements for the GFNS/AC cell were conducted in a voltage range between 0 and 3 V at various scan rates as depicted in Figure 3a. The CV performances of the GFNS/AC and GF/AC cells measured at a scan rate of 50 mV s^{-1} are compared in Figure 3b. It is clear from the Figure 3a that the CV curves of GFNS/AC cells exhibited a deviation from the rectangular shape. The appearance of a hump around 1.8 eV indicates that the measured capacitance not only is a pure double layer capacitance but also originates from the contribution of the pseudocapacitance. The electrochemical performance of the GFNS/AC cell was also measured using the galvanostatic charge/discharge (GCD) at current densities from 0.4 to 4 A/g, shown in Figure 3c. The deviation of the GCD curves from an ideal triangular shape indicates that the hybrid supercapacitor exhibits charge−discharge characteristics of a supercapacitor combined with a battery. During charging, lithium ions from the electrolyte react with Fe_2O_3 in the GFNS anode, providing the pseudocapacitance effect (battery type), and simultaneous adsorption of anions (PF^{6-}) from the electrolyte over the positive AC electrode provides the double layer capacitance effect (supercapacitor type). On the other hand, during discharging, Fe_2O_3 is regenerated, with simultaneous anionic desorption from the AC. Thus, the total capacitive response from the hybrid capacitor results from the combinatory behavior of the electric double layer charge storage occurring at the AC cathode and the redox reactions occurring at the GFNS anode. Thus, the GFNS/AC cell performs very well as a hybrid supercapacitor, which is the combination of a supercapacitor and the battery.

In order to further investigate this combinatory behavior, the electrochemical performances of the GFNS electrode and AC electrode were separately characterized in Li half-cell configurations at a scan rate of 0.1 mV/s in the potential range 0.01−3 V, as shown in Figure S5. The CV analyses of the GFNS electrode using Li half-cells (Figure S5a) depict the pseudocapacitive nature, and the charge/discharge profiles of GFNS half-cell vs Li/Li^+ at a current density of 100 mA/g is shown in Figure S5b, which also confirms the battery type

DOI: 10.1021/acsami.7b03299
ACS Appl. Mater. Interfaces 2017, 9, 22398−22407

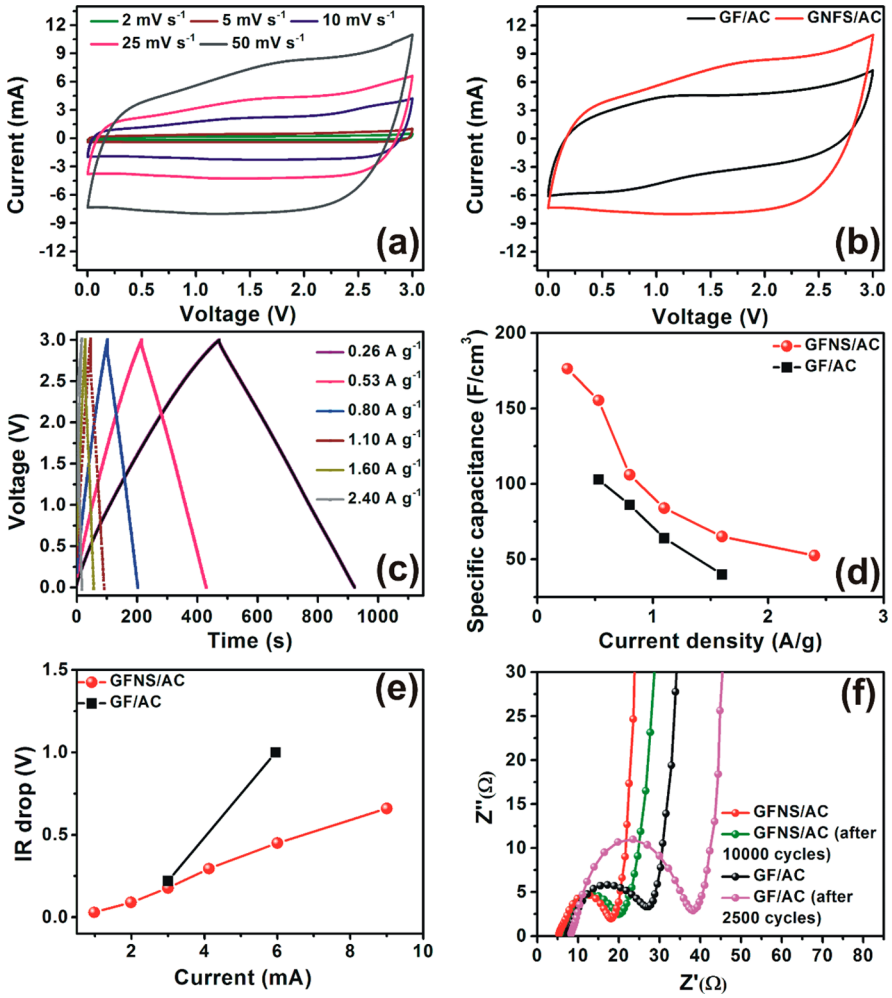

Figure 3. Electrochemical performance of the GFNS and GF electrodes in the hybrid supercapacitor: (a) CV analysis of the GFNS/AC cell at various scan rates; (b) CV curves of the GFNS/AC and GF/AC cells at a scan rate of 50 mV/s; (c) galvanostatic charge−discharge curves of the GFNS/AC hybrid supercapacitor; (d) specific capacitances of the GFNS/AC and GF/AC cells as a function of the current density; (e) Ohmic voltage (*IR*) drop for the GFNS/AC and GF/AC cells; and (f) Nyquist plots of the GFNS/AC and GF/AC cells before and after cycling in a frequency range of 100 kHz to 0.01 Hz.

behavior of the GFNS electrode. The CV analyses of the AC electrode using Li half-cells exhibit a rectangular CV shape that corresponds to double layer capacitance (Figure S5c). Figure S5d shows galvanostatic charge−discharge curves of AC. The curve is nearly a straight line, illustrating an EDLC-type supercapacitor behavior of AC. Details of the pseudocapacitive nature of the GFNS electrode has been given in the Supporting Information. Thus, the total capacitive response from the hybrid capacitor results from the combination of the electric double layer charge storage occurring at the AC cathode and the redox reactions occurring at the GFNS anode, and it performs very well as a hybrid supercapacitor with the combined mechanisms of capacitor and battery. EDLC and pseudocapacitance regions of the CV curve at a scan rate of 50 mV/s are shown in Figure S6a.

A higher output current in the GFNS than the GF cells indicates a very efficient electrolyte diffusion within the porous GFNS. The GCD performances of the GF/AC cell at various current densities are given in Supporting Information Figure S6b.

The volumetric specific capacitance (C_{vol}) can be calculated using the following equation[15,20]

$$C_{vol} = C_{gra} \times \rho \quad (1)$$

where $C_{gra} = 4\frac{i\Delta t}{m\Delta V}$ is the gravimetric specific capacitance, and i, m, Δt, and ΔV are the applied current (A), mass (g) of the active material, discharge time, and potential window, respectively.[39] The packing density of the total electrode material, i.e., ρ (g/cm^3), was calculated according to the previous report,[15] and the value was 1.05 g/cm^3.

The variations in the C_{vol} values with respect to the current density for the GFNS/AC and GF/AC cells are depicted in Figure 3d. It is observed that, in our cells, the capacitance values decrease as the current density increases. At high current density, inner areas of the active electrode become inaccessible for charge storage and, consequently, migration of the electrolytic ions are limited. This is because of the contact resistance between electrode and electrolyte ions, which is built over the active material. This contact resistance increases with an increase in current density, and thus, the ion storage occurs only over the surface of the active material at higher current density.[37,40] Therefore, an increase in current density together with a low availability of active surface area leads to the decrease in the capacitance values. One of the major factors that lead to such a decrease in capacitance value is the high mass loading.[37,40] Additionally, the poor electronic conductivity of commercial

DOI: 10.1021/acsami.7b03299
ACS Appl. Mater. Interfaces 2017, 9, 22398−22407

activated carbon also results in the decrease in the capacitance value.[37,40] We could overcome the issue of low capacitance values at high current density through the following methods. (i) Using porous/hierarchically designed/patterned current collectors, which is currently under investigation. (ii) In order to improve the electronic conductivity, a mesoporous carbon adsorption electrode could be used instead of an activated carbon electrode; however, it will increase the cost factor. (iii) The presence of binder also has an effect on the decrease in the capacitance values, as active material may lose contact with the conductive carbon and thus increases the contact resistance. Binder should be avoided during fabrication of the cells.

The volumetric power density (P_{vol}) and volumetric energy density (E_{vol}) of the hybrid supercapacitor can be calculated as follows[15,41]

$$E_{vol} = E_{gra} \times \rho \tag{2}$$

$$P_{vol} = P_{gra} \times \rho \tag{3}$$

where $E_{gra} = \frac{1}{8} C_{gra} V^2$, $P_{gra} = \frac{E_{gra}}{t}$, V is the potential window (V), I is the charge/discharge current (A), t is the discharge time (s), and m (g) is the mass of the active materials including both the anode and the cathode in the hybrid supercapacitor.[41] The calculated values of gravimetric and volumetric specific capacitance, energy and power density of the GFNS/AC cell are shown in Table S3.

The GFNS/AC cell delivered a maximum energy density of 49.66 Wh/L and a corresponding power density of 352.1 W/L. It also delivered an energy density of 6.51 Wh/L at a specific power density of 7614 W/L, while the GF/AC cell delivered a maximum energy density of 31.7 Wh/L.

A noticeable increase in the volumetric energy density values of the GFNS/AC cell was observed when it was compared with that of the GF/AC cell and those of other reported values of graphene hybrid structures. The increase in E_{vol} in the GFNS/AC cell over that of the GF/AC cell can be attributed to (i) an increase in the conductivity of the GFNS electrode, (ii) an enhancement in the electron transfer process between the electrode and electrolyte, and (iii) a faster ion transfer between the electrode and electrolyte.

The conductivity enhancement of the GFNS electrode is related to the Ohmic voltage drop (*IR* drop) in the cell. The galvanostatic charge−discharge curves began with an *IR* drop due to the internal resistance of the electrode. The *IR* drop in the cell resulted from the separation of the electrochemical double layer across the electrode/electrolyte interface and the redox component associated with the Faradaic reaction of the Fe_2O_3 electrodes. The *IR* drop against the discharge current is depicted in Figure 3e and can be used to estimate the overall cell resistance/conductivity from the slope of the *IR*−*I* plot. It is clear from Figure 3e that the slope was lower for the GFNS/AC cell than for the GF/AC cell, which confirmed that the GFNS/AC cell had a higher conductivity than the GF/AC cell, which in turn resulted in a higher C_s value. The XPS analyses revealed that the GFNSs consisted of graphitic-N atoms, which are important in the enhancement of the conductivity of the GFNS electrode.

In order to confirm the enhancement of the electron transfer process and the faster ion transfer between the electrodes and electrolyte, EIS studies were conducted for the GFNS/AC and GF/AC cells before and after cycling at a frequency range between 100 kHz and 100 MHz with an amplitude of 10 mV in open circuit conditions. The corresponding EIS spectra are presented in Figure 3f. The EIS is a powerful tool for analyzing the internal resistance of the electrode material and the resistance between the electrode and electrolyte.[42] The Nyquist spectra of both cells consisted of semicircles in the high-to-medium frequency region and a sloping line in the low frequency region. The slope of the line represents the diffusion control process in the low frequency region. In the high frequency region, the intercept of the semicircle with the real impedance axis (Z') represents the equivalent series resistance (ESR). Figure 3f clarifies that the ESR of the GFNS/AC cell (5.3 Ω) was lower than that of the GF/AC cell (7.4 Ω). The lower ESR of the GFNS/AC cell compared with that of the GF/AC cell resulted from the high conductivity of the GFNS electrode, the low contact resistance originating from the strong bonding between Fe_2O_3 and rGO, and the more active sites in the GFNS electrode between the GFNS electrode and electrolyte.

The diameter of the semicircle provides the charge transfer resistance (R_{ct}) that results from the diffusion of electrons in the electrode materials. The lower R_{ct} of the GFNS compared with that of the GF/AC cell indicates the enhancement in the electron transfer process. The scroll structure provides a connected network for the Fe_2O_3 particles. It results in a lower resistance and a shorter electron diffusion pathway, which leads to the enhanced electron transfer process.

The linear section in the low frequency region, called the Warburg resistance, represents the diffusion behavior of the electrolyte ions within the electrodes. The projected length toward Z' provides the characteristics of the ion penetration process.[43] It is apparent that the GFNS electrode has a more vertical curve than the GF electrode, which indicates that the GFNS structure has a shorter ion diffusion and better capacitor performance. For the GFNS, the diffusive line is closer to an ideally straight line, which indicates a faster ion transfer.

The low contact resistance between the electrode and electrolyte, and the abundant pores in the GFNS electrode enhance the diffusivity of the electrolyte ions and result in fast diffusion of the Li ions. Furthermore, the open and connected architecture of the conductive scrolls provides a good interface for the electrolyte ions, which increases the electrochemical accessibility of the electrolyte ions into the GFNS electrode, and this provides the short diffusion length and rapid transport of the Li ions.

A schematic of the charge/discharge process of the GFNS/AC cell is presented Figure 4a. The GFNS/AC cell exhibited stable cycling performance and maintained 88% of its initial capacitance, even after 10 000 cycles at a current density of 2.4 A g^{-1}, while the GF/AC cell exhibited inferior cyclability even at a low current density, as depicted in Figure 4b.

Figure 3f reveals that there was only a minor increase in the diameter of the semicircle of the GFNS/AC cell after 10 000 cycles. The R_{ct} value slightly increased from 12.5 to 13.6 Ω for the GFNS/AC cell after 10 000 cycles. This outstanding cycling behavior resulted from the scroll structure formed through a strong Fe_2O_3 attachment onto the rGO sheets via the nitrogen bonding. In addition, the hollow scroll structure managed the volume change that occurred in the Fe_2O_3 because the scrolls provided sufficient inner space to accommodate the large volume variation.

For the GF/AC cell, the diameter of the semicircle increased after 2000 cycles and the R_{ct} value increased from 19.3 to 29.8 Ω, as described in Figure 3f. The GFNS/AC cell exhibits the better cycling stability than the GF/AC cell, which results from the

DOI: 10.1021/acsami.7b03299
ACS Appl. Mater. Interfaces 2017, 9, 22398−22407

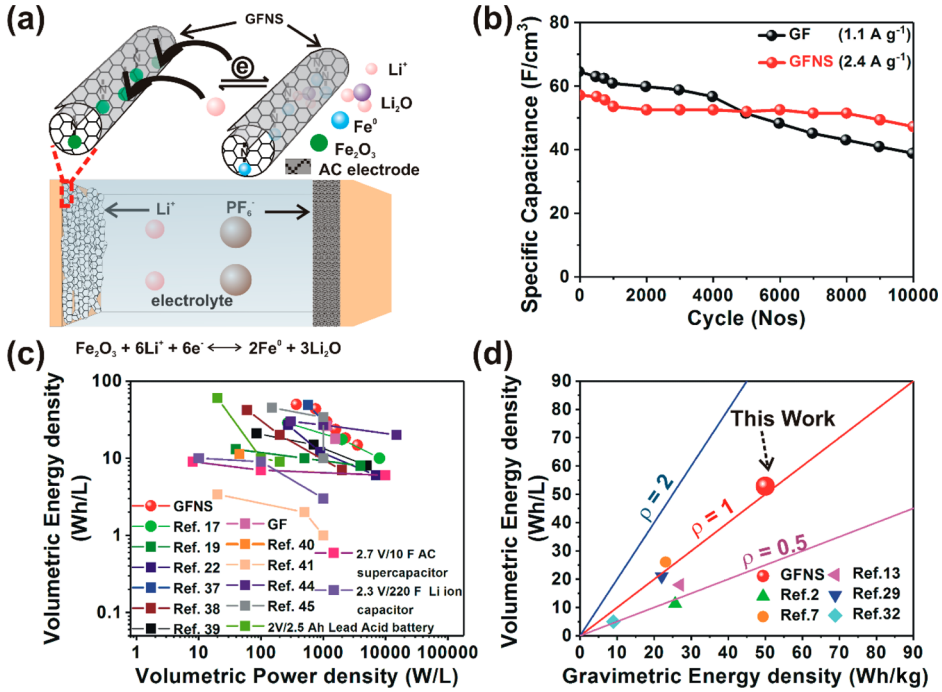

Figure 4. (a) Schematic of the discharge/charge process of the GFNS/AC cell. (b) Cycle performance of the GF/AC and GFNS/AC cells. (c) Ragone plots of the GFNS/AC cell. The corresponding values reported for recent rGO/graphene-based supercapacitors[17,19,22,44−48] are included for comparison. (d) A comparison of the volumetric and gravimetric energy densities of the GFNS/AC cell with those of the recently reported graphene-based supercapacitors.

stronger attachment of Fe_2O_3 to the rGO and the scroll structure that provides sufficient space for the volume expansion of Fe_2O_3.

The ex situ XPS spectra (C 1s, N 1s, Fe 2p) are also recorded to confirm the C−N−Fe bonding after the charge/discharge process. The fitted XPS spectra is shown in Supporting Information Figure S7, and the corresponding analysis is shown in Supporting Information Table S4. The XPS spectra and ex situ EDAX spectra of the GFNS sample after charging (Figure S8) and discharging (Figure S9) confirm that C−N−Fe bonds are well-maintained before and after the charge/discharge cycle.

The Ragone plots of the recently reported graphene-based supercapacitors are compared with those of the proposed GFNS/AC and GF/AC cells in Figure 4c. The volumetric and gravimetric energy densities of the GFNS/AC cell are compared with those of the recently reported graphene-based supercapacitors, as depicted in Figure 4d. The GFNS/AC cell exhibited a high volumetric energy density of 49.66 Wh/L and a high gravimetric energy density of 47.3 Wh/kg. In addition, the gravimetric Ragone plot of the GFNS/AC cell and those of the recently reported graphene-based supercapacitors are compared in Figure S10. It is worth pointing out that the excellent performance of the GFNS/AC cell is suitable for applications that demand both high volumetric and high gravimetric energy densities.

The volumetric energy density of the GFNS/AC cell is higher than those of the recently reported configurations, including the crumbled nitrogen-doped graphene (43 Wh/L),[49] functional pillared graphene frameworks (27 Wh/L),[22] low temperature assisted functionalized graphene (27.2 Wh/L),[50] densely porous graphene-like carbon (21 Wh/L),[46] activated carbon (44 Wh/L),[51] and single-walled carbon nanotube (47 Wh/L).[52]

The high volumetric energy density of the proposed GFNS/AC cell can be primarily ascribed to the following two aspects.

(i) The scrolls have uniformly distributed mesopores with optimum pore diameters.

The pore analyses of the GFNS samples demonstrated that the GFNS had a narrow mesopore size distribution. Because these scrolls overlap each other, the highly uniform pores function as channels for the higher transport and diffusion of ions. It should be noted that the accessibility of the mesopores to the ions depends on the pore diameter: if the ions are larger than the pore size, the ions cannot transport or diffuse through the pores. For carbon materials, large fractions of the pores have smaller sizes, which are inaccessible for ions to transport or diffuse. If the pore size is too large, a significant drop in the volumetric energy density is observed due to the ion sieving effect.[53] At a particular voltage, the energy density increased with the pore diameter, and after reaching an optimum, it began to decrease for pores with larger sizes due to the presence of an inactive electroneutral zone at the center of the large pore. From the pore size analysis of the GFNS sample, a uniform mesopore size distribution (pore diameter: 3 nm) was observed, and this enabled the superior volumetric and gravimetric performances in the GFNS/AC cell.

(ii) The scrolls have an optimum pore volume.

The electrode of a supercapacitor should be sufficiently porous to facilitate the rapid diffusion and transport of ions, and the highly porous nature of the electrodes results in a high gravimetric energy density. However, the highly porous nature of the electrodes resulted in a very low packing density. In general, the low packing density of the electrode materials causes the low volumetric energy density of the supercapacitors due to the increased amount of electrolyte required to fill the large empty spaces in the electrode. As the packing density increases, the porosity decreases due to their trade-off relationship.

DOI: 10.1021/acsami.7b03299
ACS Appl. Mater. Interfaces 2017, 9, 22398−22407

Therefore, in order to simultaneously achieve high gravimetric and volumetric energy densities in an electrode, there should be an optimum pore volume and packing density. From the BET analysis, it was found that the pore volume of the GFNS sample was low compared with that of the GF sample; therefore, the GFNS/AC cell achieved the higher packing density. Thus, the optimum pore volume and packing density of the GFNS/AC cell resulted in high gravimetric and volumetric energy densities. In order to analyze the variation in the morphology, we observed the ex situ TEM images of the GFNS samples after being subjected to 50 charging and discharging cycles, which are as shown in Figure S11a,b. Additional HRTEM images of the GFNS samples after charging and discharging cycles are also shown in Figure S12a−d. It is apparent from the figures that the samples after charging and discharging cycles exhibit similar scroll morphology. The scroll structures are maintained even after the samples are subjected to 50 charge/discharge cycles, and it is confirmed that GFNS scrolls are stable and prevent restacking of rGO layers. It can also be presumed that the porosity of both the samples (after charging and discharging) is similar.

In general, it is considered that the designed electrode architecture improved the electrochemical performance of the electrode materials and enabled these materials to obtain excellent performance for supercapacitors with high volumetric energy density and cycling stability.

4. CONCLUSIONS

A hybrid supercapacitor was designed and fabricated utilizing Fe_2O_3 encapsulated within rGO scrolls as the anode. The GFNS/AC hybrid supercapacitor exhibited high volumetric and gravimetric energy densities with a superior rate performance. The superior performance of the GFNS/AC hybrid capacitor was primarily attributed to the scroll morphology. The GFNS/AC capacitor cell had excellent cycling stability due to the protection of the conductive rGO covering, which aided in avoiding active material loss and enabled strong bonding between Fe_2O_3 and graphene via nitrogen. In the voltage range from 0 to 3.0 V, the GFNS/AC cell demonstrated a superior volumetric energy density of 49.66 Wh/L, which is comparable to those of leading acid batteries. The developed Fe_2O_3−rGO hybrid scroll structure offers significant potential as an electrode material for energy storage systems and can also be used to enhance the performance of the other electrode materials for lithium ion batteries and hybrid supercapacitors.

■ ASSOCIATED CONTENT

Supporting Information

The Supporting Information is available free of charge on the ACS Publications website at DOI: 10.1021/acsami.7b03299.

EDAX spectra; Raman spectra, pore size distribution, nitrogen adsorption/desorption plot, XRD patterns; XPS survey spectrum, C 1s, N 1s, Fe 2p XPS spectra; table showing the fitted binding energy peaks and their assignments; charge−discharge curves; electrochemical performance of GFNS electrode; table summarizing the perfomance comparison of carbon-based LIB anode materials; galvanostatic charge−discharge curves; table showing the gravimetric energy and power density values; gravimetric Ragone plot; ex-situ HRTEM images and XPS spectra of GFNS; table showing the fitted binding energy peaks and their assignments (PDF)

■ AUTHOR INFORMATION

Corresponding Author

*E-mail: jjang@gist.ac.kr.

ORCID

Yun-Sung Lee: 0000-0002-6676-2871

Jae-Hyung Jang: 0000-0001-9633-5574

Author Contributions

‖These authors contributed equally. The manuscript was written through contributions of all authors. All authors have given approval to the final version of the manuscript.

Notes

The authors declare no competing financial interest.

■ ACKNOWLEDGMENTS

This work was supported by a GIST Research Institute (GRI) project through a grant provided by GIST in 2016 and by the National Research Foundation of Korea (NRF) grant (No. 2017R1A2B3004049) funded by the Korea Government, Ministry of Science, ICT and Future Planning. This work was supported by the Technology Innovation Program (No.10053010) funded by the Ministry of Trade, industry & Energy (MI, Korea).

■ REFERENCES

(1) Choudhary, N.; Li, C.; Moore, J.; Nagaiah, N.; Zhai, L.; Jung, Y.; Thomas, J. Asymmetric Supercapacitor Electrodes and Devices. *Adv. Mater.* **2017**, *29*, 1605336.

(2) Ji, B.; Zhang, F.; Song, X.; Tang, Y. A Novel Potassium-Ion-Based Dual-Ion Battery. *Adv. Mater.* **2017**, *29*, 1700519.

(3) Qin, P.; Wang, M.; Li, N.; Zhu, H.; Ding, X.; Tang, Y. Bubble-Sheet-Like Interface Design with an Ultrastable Solid Electrolyte Layer for High-Performance Dual-Ion Batteries. *Adv. Mater.* **2017**, *29*, 1606805.

(4) Sheng, M.; Zhang, F.; Ji, B.; Tong, X.; Tang, Y. A Novel Tin-Graphite Dual-Ion Battery Based on Sodium-Ion Electrolyte with High Energy Density. *Adv. Energy Mater.* **2017**, *7*, 1601963.

(5) Tong, X.; Zhang, F.; Ji, B.; Sheng, M.; Tang, Y. Carbon-Coated Porous Aluminum Foil Anode for High-Rate, Long-Term Cycling Stability, and High Energy Density Dual-Ion Batteries. *Adv. Mater.* **2016**, *28*, 9979−9985.

(6) Zhang, X.; Tang, Y.; Zhang, F.; Lee, C.-S. A Novel Aluminum−Graphite Dual-Ion Battery. *Adv. Energy Mater.* **2016**, *6*, 1502588.

(7) Ji, B.; Zhang, F.; Sheng, M.; Tong, X.; Tang, Y. A Novel and Generalized Lithium-Ion-Battery Configuration utilizing Al Foil as Both Anode and Current Collector for Enhanced Energy Density. *Adv. Mater.* **2017**, *29*, 1604219.

(8) Thangavel, R.; Kaliyappan, K.; Kang, K.; Sun, X.; Lee, Y.-S. Going Beyond Lithium Hybrid Capacitors: Proposing a New High-Performing Sodium Hybrid Capacitor System for Next-Generation Hybrid Vehicles Made with Bio-Inspired Activated Carbon. *Adv. Energy Mater.* **2016**, *6*, 1502199.

(9) Thangavel, R.; Moorthy, B.; Kim, D. K.; Lee, Y.-S. Pushing the Energy Output and Cyclability of Sodium Hybrid Capacitors at High Power to New Limits. *Adv. Energy Mater.* **2017**, 1602654.

(10) Li, F.; Jiang, X.; Zhao, J.; Zhang, S. Graphene Oxide: A Promising Nanomaterial for Energy and Environmental Applications. *Nano Energy* **2015**, *16*, 488−515.

(11) Liu, J.; Lu, P.-J.; Liang, S.; Wang, W.; Lei, M.; Tang, S.; Yang, Q.; Liu, J. Ultrathin Li_3VO_4 Nanoribbon/Graphene Sandwich-like Nanostructures with Ultrahigh Lithium Ion Storage Properties. *Nano Energy* **2015**, *12*, 709−724.

(12) Simon, P.; Gogotsi, Y. Materials for Electrochemical Capacitors. *Nat. Mater.* **2008**, *7*, 845−854.

(13) Zhang, S.; Zhu, L.; Song, H.; Chen, X.; Zhou, J. Enhanced Electrochemical Performance of MnO Nanowire/Graphene Compo-

DOI: 10.1021/acsami.7b03299
ACS Appl. Mater. Interfaces 2017, 9, 22398−22407

site During Cycling as the Anode Material for Lithium-Ion Batteries. *Nano Energy* **2014**, *10*, 172−180.
(14) Yu, D.; Goh, K.; Zhang, Q.; Wei, L.; Wang, H.; Jiang, W.; Chen, Y. Controlled Functionalization of Carbonaceous Fibers for Asymmetric Solid-State Micro-Supercapacitors with High Volumetric Energy Density. *Adv. Mater.* **2014**, *26*, 6790−6797.
(15) Sheng, L.; Jiang, L.; Wei, T.; Fan, Z. High Volumetric Energy Density Asymmetric Supercapacitors Based on Well-Balanced Graphene and Graphene-MnO_2 Electrodes with Densely Stacked Architectures. *Small* **2016**, *12*, 5217−5227.
(16) Jiang, L.; Sheng, L.; Long, C.; Fan, Z. Densely Packed Graphene Nanomesh-Carbon Nanotube Hybrid Film for Ultra-High Volumetric Performance Supercapacitors. *Nano Energy* **2015**, *11*, 471−480.
(17) Long, C.; Jiang, L.; Wu, X.; Jiang, Y.; Yang, D.; Wang, C.; Wei, T.; Fan, Z. Facile Synthesis of Functionalized Porous Carbon with Three-Dimensional Interconnected Pore Structure for High Volumetric Performance Supercapacitors. *Carbon* **2015**, *93*, 412−420.
(18) Cao, X.; Yin, Z.; Zhang, H. Three-Dimensional Graphene Materials: Preparation, Structures and Application in Supercapacitors. *Energy Environ. Sci.* **2014**, *7*, 1850−1865.
(19) Tao, Y.; Xie, X.; Lv, W.; Tang, D.-M.; Kong, D.; Huang, Z.; Nishihara, H.; Ishii, T.; Li, B.; Golberg, D.; Kang, F.; Kyotani, T.; Yang, Q.-H. Towards Ultrahigh Volumetric Capacitance: Graphene Derived Highly Dense but Porous Carbons for Supercapacitors. *Sci. Rep.* **2013**, *3*, 2975.
(20) Pham, V. H.; Dickerson, J. H. Reduced Graphene Oxide Hydrogels Deposited in Nickel Foam for Supercapacitor Applications: Toward High Volumetric Capacitance. *J. Phys. Chem. C* **2016**, *120*, 5353−5360.
(21) Xu, Y.; Lin, Z.; Zhong, X.; Huang, X.; Weiss, N. O.; Huang, Y.; Duan, X. Holey Graphene Frameworks for Highly Efficient Capacitive Energy Storage. *Nat. Commun.* **2014**, *5*, 4554.
(22) Jiang, L.; Sheng, L.; Long, C.; Wei, T.; Fan, Z. Functional Pillared Graphene Frameworks for Ultrahigh Volumetric Performance Supercapacitors. *Adv. Energy Mater.* **2015**, *5*, 1500771.
(23) Braga, S. F.; Coluci, V. R.; Legoas, S. B.; Giro, R.; Galvão, D. S.; Baughman, R. H. Structure and Dynamics of Carbon Nanoscrolls. *Nano Lett.* **2004**, *4*, 881−884.
(24) Schaper, A. K.; Wang, M. S.; Xu, Z.; Bando, Y.; Golberg, D. Comparative Studies on the Electrical and Mechanical Behavior of Catalytically Grown Multiwalled Carbon Nanotubes and Scrolled Graphene. *Nano Lett.* **2011**, *11*, 3295−3300.
(25) Zhou, W.; Liu, J.; Chen, T.; Tan, K. S.; Jia, X.; Luo, Z.; Cong, C.; Yang, H.; Li, C. M.; Yu, T. Fabrication of Co_3O_4-Reduced Graphene Oxide Scrolls for High-Performance Supercapacitor Electrodes. *Phys. Chem. Chem. Phys.* **2011**, *13*, 14462−14465.
(26) Yan, C.; Xi, W.; Si, W.; Deng, J.; Schmidt, O. G. Highly Conductive and Strain-Released Hybrid Multilayer Ge/Ti Nanomembranes with Enhanced Lithium-Ion-Storage Capability. *Adv. Mater.* **2013**, *25*, 539−544.
(27) Zhang, L.; Deng, J.; Liu, L.; Si, W.; Oswald, S.; Xi, L.; Kundu, M.; Ma, G.; Gemming, T.; Baunack, S.; Ding, F.; Yan, C.; Schmidt, O. G. Hierarchically Designed SiO_x/SiO_y Bilayer Nanomembranes as Stable Anodes for Lithium Ion Batteries. *Adv. Mater.* **2014**, *26*, 4527−4532.
(28) Marcano, D. C.; Kosynkin, D. V.; Berlin, J. M.; Sinitskii, A.; Sun, Z.; Slesarev, A.; Alemany, L. B.; Lu, W.; Tour, J. M. Improved Synthesis of Graphene Oxide. *ACS Nano* **2010**, *4*, 4806−4814.
(29) Mirsaidov, U.; Mokkapati, V. R. S. S.; Bhattacharya, D.; Andersen, H.; Bosman, M.; Ozyilmaz, B.; Matsudaira, P. Scrolling Graphene into Nanofluidic Channels. *Lab Chip* **2013**, *13*, 2874−2878.
(30) Rani, J. R.; Oh, S.-I.; Woo, J. M.; Tarwal, N. L.; Kim, H.-W.; Mun, B. S.; Lee, S.; Kim, K.-J.; Jang, J.-H. Graphene Oxide−Phosphor Hybrid Nanoscrolls with High Luminescent Quantum Yield: Synthesis, Structural, and X-ray Absorption Studies. *ACS Appl. Mater. Interfaces* **2015**, *7*, 5693−5700.
(31) Li, X.; Qi, W.; Mei, D.; Sushko, M. L.; Aksay, I.; Liu, J. Functionalized Graphene Sheets as Molecular Templates for Controlled Nucleation and Self-Assembly of Metal Oxide-Graphene Nanocomposites. *Adv. Mater.* **2012**, *24*, 5136−5141.
(32) Chaudhari, S.; Bhattacharjya, D.; Yu, J.-S. 1-Dimensional Porous $\alpha-Fe_2O_3$ Nanorods as High Performance Electrode Material for Supercapacitors. *RSC Adv.* **2013**, *3*, 25120−25128.
(33) Rani, J. R.; Oh, S.-I.; Woo, J. M.; Jang, J.-H. Low Voltage Resistive Memory Devices Based on Graphene Oxide−Iron Oxide Hybrid. *Carbon* **2015**, *94*, 362−368.
(34) Rani, J. R.; Oh, S.-I.; Jang, J.-H. Raman Spectra of Luminescent Graphene Oxide (GO)-Phosphor Hybrid Nanoscrolls. *Materials* **2015**, *8*, 8460−8466.
(35) Frost, R. L.; Musumeci, A. W.; Bouzaid, J.; Adebajo, M. O.; Martens, W. N.; Theo Kloprogge, J. Intercalation of Hydrotalcites with Hexacyanoferrate(II) and (III)—A ThermoRaman Spectroscopic Study. *J. Solid State Chem.* **2005**, *178*, 1940−1948.
(36) Wu, N.; Wang, Y.; Lei, Y.; Wang, B.; Han, C.; Gou, Y.; Shi, Q.; Fang, D. Electrospun Interconnected Fe-N/C Nanofiber Networks as Efficient Electrocatalysts for Oxygen Reduction Reaction in Acidic Media. *Sci. Rep.* **2015**, *5*, 17396.
(37) Aravindan, V.; Gnanaraj, J.; Lee, Y.-S.; Madhavi, S. Insertion-Type Electrodes for Nonaqueous Li-Ion Capacitors. *Chem. Rev.* **2014**, *114*, 11619−11635.
(38) Karthikeyan, K.; Amaresh, S.; Lee, S. N.; Aravindan, V.; Lee, Y. S. Fluorine-Doped Fe_2O_3 as High Energy Density Electroactive Material for Hybrid Supercapacitor Applications. *Chem. - Asian J.* **2014**, *9*, 852−857.
(39) Fan, L.-Q.; Liu, G.-J.; Wu, J.-H.; Liu, L.; Lin, J.-M.; Wei, Y.-L. Asymmetric Supercapacitor Based on Graphene Oxide/Polypyrrole Composite and Activated Carbon Electrodes. *Electrochim. Acta* **2014**, *137*, 26−33.
(40) Amaresh, S.; Karthikeyan, K.; Jang, I. C.; Lee, Y. S. Single-Step Microwave Mediated Synthesis of the CoS_2 Anode Material for High Rate Hybrid Supercapacitors. *J. Mater. Chem. A* **2014**, *2*, 11099−11106.
(41) Shao, Y.; El-Kady, M. F.; Lin, C.-W.; Zhu, G.; Marsh, K. L.; Hwang, J. Y.; Zhang, Q.; Li, Y.; Wang, H.; Kaner, R. B. 3D Freeze-Casting of Cellular Graphene Films for Ultrahigh-Power-Density Supercapacitors. *Adv. Mater.* **2016**, *28*, 6719−6726.
(42) Wang, D.; Choi, D.; Li, J.; Yang, Z.; Nie, Z.; Kou, R.; Hu, D.; Wang, C.; Saraf, L. V.; Zhang, J.; Aksay, I. A.; Liu, J. Self-Assembled TiO_2−Graphene Hybrid Nanostructures for Enhanced Li-Ion Insertion. *ACS Nano* **2009**, *3*, 907−914.
(43) Cai, J.; Niu, H.; Li, Z.; Du, Y.; Cizek, P.; Xie, Z.; Xiong, H.; Lin, T. High-Performance Supercapacitor Electrode Materials from Cellulose-Derived Carbon Nanofibers. *ACS Appl. Mater. Interfaces* **2015**, *7*, 14946−14953.
(44) Moosavifard, S. E.; Shamsi, J.; Altafi, M. K.; Moosavifard, Z. S. All-Solid State, Flexible, High-Energy Integrated Hybrid Micro-Supercapacitors Based on 3D LSG/$CoNi_2S_4$ Nanosheets. *Chem. Commun.* **2016**, *52*, 13140−13143.
(45) El-Kady, M. F.; Ihns, M.; Li, M.; Hwang, J. Y.; Mousavi, M. F.; Chaney, L.; Lech, A. T.; Kaner, R. B. Engineering Three-Dimensional Hybrid Supercapacitors and Microsupercapacitors for High-Performance Integrated Energy Storage. *Proc. Natl. Acad. Sci. U. S. A.* **2015**, *112*, 4233−4238.
(46) Long, C.; Chen, X.; Jiang, L.; Zhi, L.; Fan, Z. Porous Layer-Stacking Carbon Derived from In-built Template in Biomass for High Volumetric Performance Supercapacitors. *Nano Energy* **2015**, *12*, 141−151.
(47) Yan, J.; Wang, Q.; Lin, C.; Wei, T.; Fan, Z. Interconnected Frameworks with a Sandwiched Porous Carbon Layer/Graphene Hybrids for Supercapacitors with High Gravimetric and Volumetric Performances. *Adv. Energy Mater.* **2014**, *4*, 1400500.
(48) Wang, Z.; Tammela, P.; Stromme, M.; Nyholm, L. Nanocellulose Coupled Fexible Polypyrrole@Graphene Oxide Composite Paper Electrodes with High Volumetric Capacitance. *Nanoscale* **2015**, *7*, 3418−3423.
(49) Wang, J.; Ding, B.; Xu, Y.; Shen, L.; Dou, H.; Zhang, X. Crumpled Nitrogen-Doped Graphene for Supercapacitors with High

DOI: 10.1021/acsami.7b03299
ACS Appl. Mater. Interfaces 2017, 9, 22398−22407

Gravimetric and Volumetric Performances. *ACS Appl. Mater. Interfaces* **2015**, *7*, 22284−22291.
(50) Yan, J.; Wang, Q.; Wei, T.; Jiang, L.; Zhang, M.; Jing, X.; Fan, Z. Template-Assisted Low Temperature Synthesis of Functionalized Graphene for Ultrahigh Volumetric Performance Supercapacitors. *ACS Nano* **2014**, *8*, 4720−4729.
(51) Kim, T.; Jung, G.; Yoo, S.; Suh, K. S.; Ruoff, R. S. Activated Graphene-Based Carbons as Supercapacitor Electrodes with Macro- and Mesopores. *ACS Nano* **2013**, *7*, 6899−6905.
(52) Izadi-Najafabadi, A.; Yasuda, S.; Kobashi, K.; Yamada, T.; Futaba, D. N.; Hatori, H.; Yumura, M.; Iijima, S.; Hata, K. Extracting the Full Potential of Single-Walled Carbon Nanotubes as Durable Supercapacitor Electrodes Operable at 4 V with High Power and Energy Density. *Adv. Mater.* **2010**, *22*, E235−E241.
(53) Wang, Q.; Yan, J.; Fan, Z. Carbon Materials for High Volumetric Performance Supercapacitors: Design, Progress, Challenges and Opportunities. *Energy Environ. Sci.* **2016**, *9*, 729−762.

DOI: 10.1021/acsami.7b03299
ACS Appl. Mater. Interfaces 2017, 9, 22398−22407